Editors' Suggestion

# Bending transition in the penetration of a flexible intruder in a two-dimensional dense granular medium

Nicolas Algarra,[1] Panagiotis G. Karagiannopoulos,[1] Arnaud Lazarus,[2] Damien Vandembroucq,[1] and Evelyne Kolb[1,*]

[1]*Laboratoire PMMH, UMR 7636 CNRS/ESPCI Paris/PSL Research University/Sorbonne Universités, UPMC Univ Paris 06,/Univ Paris Diderot, 10 rue Vauquelin, 75231 Paris cedex 05, France*

[2]*Sorbonne Universités, UPMC Univ Paris 06, CNRS, UMR 7190, Institut Jean Le Rond d'Alembert, F-75005, Paris, France*

(Received 4 August 2017; published 5 February 2018)

We study the quasistatic penetration of a flexible beam into a two-dimensional dense granular medium lying on a horizontal plate. Rather than a buckling-like behavior we observe a transition between a regime of crack-like penetration in which the fiber only shows small fluctuations around a stable straight geometry and a bending regime in which the fiber fully bends and advances through series of loading and unloading steps. We show that the shape reconfiguration of the fiber is controlled by a single nondimensional parameter $L/L_c$, which is the ratio of the length of the flexible beam $L$ to $L_c$, a bending elastogranular length scale that depends on the rigidity of the fiber and on the departure from the jamming packing fraction of the granular medium. We show, moreover, that the dynamics of the bending transition in the course of the penetration experiment is gradual and is accompanied by a symmetry breaking of the granular packing fraction in the vicinity of the fiber. Together with the progressive bending of the fiber, a cavity grows downstream of the fiber and the accumulation of grains upstream of the fiber leads to the development of a jammed cluster of grains. We discuss our experimental results in the framework of a simple model of bending-induced compaction and we show that the rate of the bending transition only depends on the control parameter $L/L_c$.

DOI: 10.1103/PhysRevE.97.022901

## I. INTRODUCTION

Slender structures are extremely flexible and get easily unstable. The ratio of the bending stiffness of a beam to its axial stiffness in tension or compression scales with $(t/L)^2$, the square of the ratio of the thickness to the length of the beam [1]. Similarly, over a threshold compressive strain of order $(t/L)^2$, the beam undergoes a buckling instability [2]. As a consequence of their high geometrical aspect ratio, slender structures can be sensitive to low forces of various origins and exhibit complex mechanical behavior due to the associated couplings. This is, in particular, the case of the elastocapillary problems (interactions between slender structures and capillary forces) which have raised a growing interest in the recent years [3].

In the same spirit, the effect of flexibility on fluid-structure interactions has recently motivated a growing number of studies at low [4,5] or high Reynolds number [6]. Model experiments of reconfigurations have been performed with flexible fibers [one-dimensional (1D)], plates [two-dimensional (2D)], or assemblies of plates organized in a circular pattern [three-dimensional (3D)] that were placed initially perpendicular to the incoming flow of air [7], water [8], or 2D soap film [9]. In all these cases, the flexible body experiences shape reconfiguration with self-streamlining and reduction of the surface area exposed to the flow, thus resulting in a drastic reduction of the drag force exerted on the object [10]. An immediate field of application of these problems can be found in biophysical domains, when a passive or an active elastic part of a body interacts with the flow [6,11–13]. In particular, in animal locomotion, the flexibility of wings or fins intervene in the flying of birds and insects or the swimming of fish or eels. Even in microorganisms the propulsion through flagella takes advantage of the flexibility. Numerous examples can also be found in the plant domain [14] where the flexibility of cereal stems, tree trunks, branches, or leaves can be beneficial under wind flow for reducing lodging. Even marine algae and plants in aquatic canopies adapt their shape under water current [15,16].

Here we consider an original case of fluid-structure interaction between a slender structure and a granular medium. More specifically, we study the quasistatic penetration of a flexible beam into a two-dimensional dense bidisperse mixture of discs lying on a plate. Applications of this problem range from nuclear engineering [17] to biology: the growth of roots [18,19] in structured soils or the locomotion of worms or sandfish lizards in granular media [20].

The complex behavior of granular flows has recently been studied through its interaction with rigid intruders [21–33]. The high sensitivity of flexible intruders to low forces opens here a promising new way of probing the mechanical behavior of granular media [34–36]. The complexity of such a question of *elastogranular mechanics* (as recently coined in Ref. [35]) will naturally arise from the coupling of the low rigidity of the elastic beam with the discrete nature of the granular flow, its nonlocal rheology [37], and the emergence of turbulent-like fluctuations [38–40] in the vicinity of the jamming transition.

In contrast with two recent works focusing on buckling [34,35], the present study will highlight a bending transition of the flexible intruder and an associated transition in the structure of the granular medium.

In the following we first give in Sec. II a brief description of the experimental setup and tools of analysis; we then discuss

*https://orcid.org/0000-0002-5346-6635

 

in Sec. III the phenomenology of the interaction between an elastic beam and a granular flow, we report our experimental observation of bistability between two different regimes (straight or bent fiber), we identify the control parameters (rigidity of the fiber and packing fraction of the granular medium) and propose a simple model. In Sec. IV we focus specifically on the development of the bending transition and show that it is associated with a clear symmetry breaking of both the geometry of the fiber and the density of the granular material in the vicinity of the fiber. We then propose in Sec. V a model of bending-induced compaction that allows us to reasonably reproduce the evolution of the fiber deflection in the course of the bending transition. A summary of our main results is finally given in Sec. VI.

## II. EXPERIMENTAL SETUP

### A. Granular medium

The 2D granular material is a bidisperse mixture of brass cylinders, in equal-mass proportion, forming a dense and disordered assembly of rigid disks [27,28]. The small cylinders of number $N_1$ have an outer diameter $d_1 = 4$ mm, an inner diameter of 2.2 mm, and a mass of 0.209 g whereas the large cylinders of number $N_2 = \frac{4}{7}N_1$ have an outer diameter $d_2 = 5$ mm, an inner diameter of 2.5 mm, and a mass of 0.363 g. Choosing grains as empty cylinders with different internal diameters helps in distinguishing between large and small grains for pattern recognition during image analysis. The choice of the two close external diameters and the proportion between small and large grains were chosen to reduce segregation between the two populations of grains. This collection of grains lies on a horizontal glass plate delimited by four brass walls forming a rectangular frame of width $W = 269.5$ mm ($54d_2$ along the $X$ axis) and adjustable length $H$ along the $Y$ axis (Fig. 1). The total number of cylinders is kept constant around 6800, but as we varied $H$ in the range 457.5 mm ($91d_2$) to 470.5 mm ($94d_2$), we could adjust the total available cell surface and therefore the packing fraction $\phi$. In the following experiments, the packing fraction $\phi$ varies between 80.85% and 83.1%, just below the assumed jamming packing fraction, $\phi_J = 83.56\% \pm 0.08\%$. This value of $\phi_J$ was determined from a preceding similar experiment where a rigid obstacle (cylindrical intruder) was in place of the flexible one [27]. Before each experiment, grains are carefully mixed such that the topological organization of grains is changed without inducing segregation.

The measurement of the static grain-grain friction coefficient gives $\mu_{gg} = 0.32 \pm 0.07$ [41], while the one for the frictional contact of grains with the glass bottom leads to $\mu = \mu_{gb} = 0.49 \pm 0.09$. The static coefficient of friction $\mu$ is obtained from the tangent of the angle at which the incipient sliding of a grain on a progressively tilted glass surface occurs. In the following, we use the notation $d = \frac{N_1 d_1 + N_2 d_2}{N_1 + N_2} = 4.36$ mm and $m = \frac{N_1 m_1 + N_2 m_2}{N_1 + N_2} = 0.265$ g for the weighted average of grain external diameter and mass, respectively. We also define an effective density of the grains as $\rho = \frac{m}{sh}$ where $s = \frac{\pi}{4}\frac{N_1 d_1^2 + N_2 d_2^2}{N_1 + N_2}$ is the weighted average surface occupied by one grain on the bottom glass plate. This effective density $\rho = 5835 \pm 5$ kg/m$^3$ takes into account the fact that grains are hollow cylinders.

### B. The flexible beam

The flexible beam is cut into a mylar sheet of thickness $t = 350\,\mu$m, Young's modulus $E = 3.8$ GPa, and Poisson ratio $\nu = 0.4$ [42]. The flexible part of the intruder is a long beam, that we will call "fiber," of length $L$ with a rectangular cross section defined by the sheet thickness $t$ and a height $h = 3$ mm corresponding to the height of the cylinders of the granular material. One of the intruder extremities is clamped into a rigid metallic part supported by a transverse arm along the $X$ plane (Fig. 1). The other fiber extremity is free.

The anchoring point of the intruder is fixed in the laboratory frame and is located at an equal distance of the two lateral walls delimiting the space for the granular layer. The basis of the fiber is fixed slightly above the bottom glass plate, so that there is no friction with the bottom. At the beginning of the experiment, the fiber is straight along the $Y$ axis with no contact with neighboring grains. The anchoring point of the fiber is initially located at a distance of 80 mm = $16d_2$ (or 120 mm = $24d_2$ depending on the batch of experiments) from the back wall, to avoid boundary effects. In this work, we used different fiber lengths between $L = 1$ cm and $L = 5$ cm.

### C. Principle of the experiment

A typical experiment consists in translating the granular material supported by the glass plate along the $Y$ axis against the free extremity of the fiber. The plate velocity $V_0$ is held constant. In the plate frame this is equivalent of having a fiber penetrating the granular material at a constant velocity $V_0$. The experiment is stopped after a plate displacement of typically 260 mm ($52d_2$).

The velocity of the plate was always kept constant at $V_0 = 5/6$ mm/s. This value corresponds to a quasistatic regime in which the forces are dominated by frictional contact forces. Actually we observe that the drag force experienced by a rigid cylindrical intruder does not depend on velocity in these ranges of values. A CCD camera of $1600 \times 1200$ pixels placed above the setup records images at a frequency of 2 Hz, corresponding to a plate displacement of $U_0 = 5/12$ mm $= d_2/12$ between two successive images. Ten similar experiments are performed for each set of parameters $L$ and $\phi$, and grains are carefully remixed between two consecutive experiments. At the end of an experiment, the bending of the fiber can be so large that the fiber undergoes plastic deformation at the anchoring point. In this case, we replace the fiber by a new one.

### D. Segmentation and image processing

For all images of each batch of experiments, a technique of correlation on gray levels has been used for determining the grain centers with a subpixel accuracy. Then the grain displacements from one image to the next are computed. Furthermore, the full deflected shape of the fiber is obtained for most images. The delicate challenge for image analysis was to locate the very thin and elongated fiber among the circular grains surrounding it. For this purpose, the gray-level image has been convoluted with different filters to enhance the contrast of the fiber and disconnect it from the neighboring grains. This first step gave a skeleton of the fiber, which was further fully reconstructed by starting from the fiber anchoring point. From

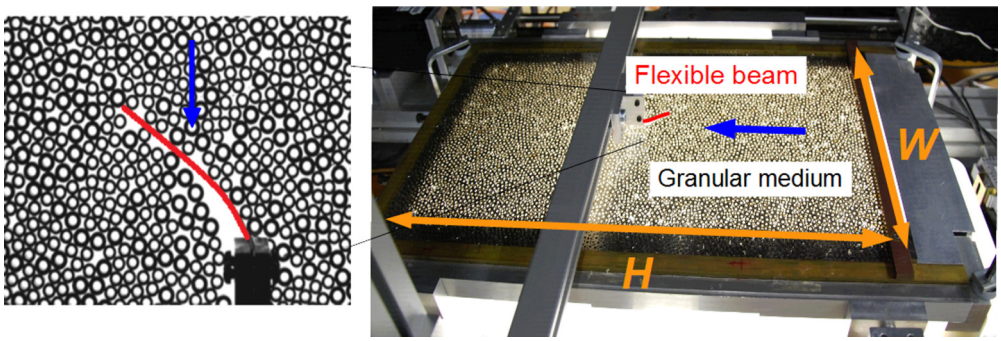


FIG. 1. Experimental setup (right panel): the granular layer is contained in an horizontal rectangular plate of width $W$ and length $H$ that moves at a constant speed along the direction indicated by the blue arrow ($Y$ axis). Bending of the fiber (left panel) produced by the granular flow as observed in a zoom of a picture taken with a CCD camera placed above the setup. The fiber clamping point is fixed in the laboratory frame.

the fiber shape, different information can be obtained, such as the free-end lateral deflection $\delta$ or the local slope $\theta$ of the fiber relative to the $Y$ axis. This local slope can be computed as a function of the curvilinear abscissa $\xi$ (normalized by the length of the fiber), with $\xi = 0$ at the clamped extremity and $\xi = 1$ at the free extremity.

## III. PHENOMENOLOGY: FLUID-STRUCTURE INTERACTION IN A GRANULAR FLOW

When immersed in a fluid, a flexible structure interacts with the flow. In particular, depending on the rigidity of the structure and the flow conditions, it can switch from the initial undeformed configuration to a deformed configuration that reduces the drag force. Alternatively, for a given bending rigidity, there exists a critical length of the structure placed across the flow above which reconfiguration occurs.

A very similar phenomenology can be observed in the present experiment which can be regarded as an interaction between a flexible beam and a granular flow. In Fig. 2(a) we show a series of configurations of a short (rigid) fiber ($L =$ 2 cm) facing the granular flow. Small fluctuations are observed around the stable straight configuration, as if the fiber was jiggling around its initial position. The slight deflections are here caused by collisions with incoming grains. In Fig. 2(b) we show the contrasting case of a slightly longer fiber ($L = 3$ cm) for the same granular packing fraction as before. In this case, the fiber experiences reconfiguration due to the flow and enters into a regime of bending.

When the 3-cm-long fiber has been highly tilted, fluctuations of the fiber positions are again observed but of a very different nature: in Fig. 3(a) we show the gradual bending of the deformed fiber due to an accumulation of incoming grains and in Fig. 3(b) its sudden partial recovery. In Fig. 4, we represent the corresponding grain displacements in the plate frame (by subtracting the plate displacement $U_0$ between two consecutive images) as if the fiber was penetrating the granular material. Figure 4(a) shows the displacement field between the two images just before the unloading event. It is characterized by long-range displacements in front of the fiber and small recirculations on both sides. Figure 4(b) shows the displacement field corresponding to the unloading phase, with the fiber returning from position B to position C. In contrast with the loading phase, the elastic return of the fiber is associated with huge recirculations on both sides. Therefore the sudden change of the fiber conformation can be associated with a large reconfiguration of the grains, in other words a burst of the velocity field of the granular flow. Such an alternation of smooth and regular loading stages interspersed with sudden unloading events is typical of granular avalanches and can also be associated with the turbulent-like velocity fluctuations reported in dense granular flows [38–40].

In Fig. 5 we summarize our observations of the straight (jiggling regime) or deformed conformation (bending regime)

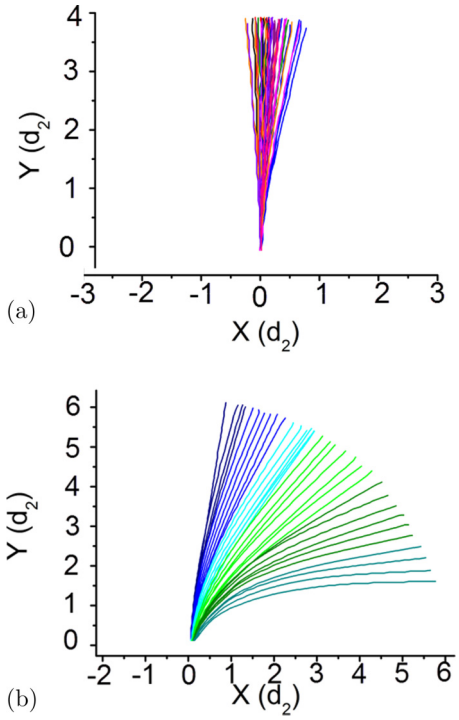


FIG. 2. (a) Fluctuations of an elastic beam of length $L = 2$ cm in a granular medium of packing fraction $\phi = 80.94\%$ (jiggling regime). The clamping point of the fiber is located at (0,0). The granular flow direction is along decreasing $Y$ axis. (b) Gradual bending of an elastic beam of longer length $L = 3$ cm (bending regime). The granular packing fraction is the same as in panel (a).

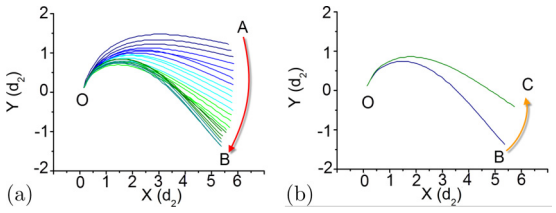


FIG. 3. Individual avalanche, loading and unloading of a fiber of length $L = 3$ cm in a granular medium of packing fraction $\phi = 80.94\%$ for a highly bent configuration (regime III). (a) Successive fiber shapes during a loading phase (plate displacement of $2U_0 = d_2/6$ between each fiber shape from A to B). (b) Unloading phase from B to C with a sudden elastic return of the fiber during one increment $U_0$ of plate displacement.

of the fiber when varying its length $L$ as well as the packing fraction $\phi$ of the granular medium.

In the present experiment, the flexible structure is initially facing the flow in a geometry of penetration. Therefore one would naturally introduce the critical force for fiber buckling. In the case of a nonembedded fiber, this force is given by the Euler force $F_C$ with clamp-free extremities. It drastically depends on the fiber length $L$ as

$$F_C(L) = \frac{\pi^2}{4}\frac{EI}{L^2}, \tag{1}$$

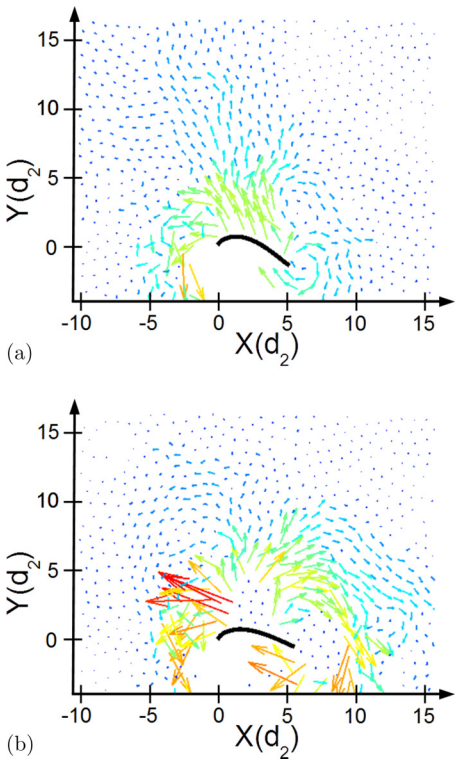


FIG. 4. Map of the displacement field of grains (amplified by a factor of 20) in the plate frame between two consecutive images for the loading and for the unloading phases of Fig. 3. The plate displacement $U_0$ between two consecutive images has been subtracted from each grain displacement. (a) Between the two images just before the unloading event; (b) during the avalanche BC.

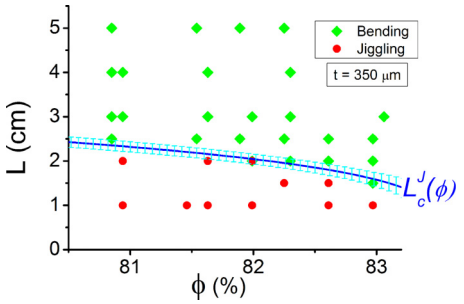


FIG. 5. Phase diagram in the plane $L$-$\phi$. Experiments vs prediction. The symbols represent the experiments performed by varying the fiber length $L$ or granular packing fraction $\phi$ with green diamonds for the bending regime and red circles for the jiggling regime. The blue curve is the predicted elastogranular length from Eq. (9) that separates the jiggling from the bending regimes with the associated error bars.

where $I$ is the quadratic moment of the fiber corresponding to a nonembedded fiber buckling in the $(X,Y)$ plane. Taking into account the rectangular cross section of the fiber yields $I = \frac{h\,t^3}{12}$. Thus, varying $L$ is a way to vary the maximum acceptable loading force (or equivalently the maximum penetrative force) in a case of a pure axial loading. For example, the typical bending rigidity for a beam of length $L = 3$ cm and thickness $t = 350\,\mu$m is $EI = 4.07 \times 10^{-5}$ N m$^2$ and the corresponding Euler force would be $F_C(L) \approx 0.11$ N. For comparison, the bending force produced by the fiber tip displacement over a distance $\delta$ is

$$F_b(L,\alpha) = \frac{\alpha EI\delta}{L^3}, \tag{2}$$

with $\alpha = 3$ for a force only acting at the tip perpendicularly to the fiber and $\alpha = 8$ for a perpendicular force homogeneously distributed over the fiber length. Thus the bending force will be $F_b(L) \approx 0.02$ N for a fiber length $L = 3$ cm and a fiber tip displacement produced by one grain size $d$ (the typical size of obstacle encountered by the fiber), that is $\delta = d$ and $\alpha = 3$. This value of $F_b(L)$ is much smaller than the corresponding buckling force for the same geometrical parameters of the fiber. In any cases, the thickness $t$ of the fiber is small compared with the diameter $d$ of a grain with $t/d \approx 0.08$, such that the probability of a force purely acting along the axis of the beam will be negligible. Therefore the main mechanism producing reconfiguration of the fiber will be attributed to bending and not buckling, contrary to the recent experiment of Ref. [34].

In studies of interactions between fluids and flexible structures it is customary to design a nondimensional number that compares drag and elastic restoring forces in order to determine the stability of the flexible object [5,7]. In the present context, a first naive scaling analysis may consist of building such a Cauchy-like number from the comparison between the friction force associated with the contact between the bottom plate and an individual grain. Thus the friction force is $f_n = \mu\rho g\pi d^2 h/4$ where $\rho$ is the effective density of an average grain of diameter $d$ and $\mu$ is the static coefficient of friction between the basis of a grain and the glass bottom plate as defined in Sec. II. The bending force associated with a deflection $\delta$ of the tip of the fiber equivalent to one grain size $d$ is given by Eq. (2) with $f_b = F_b(L,\alpha = 3)$, such that the corresponding Cauchy-like

number is written as

$$c_Y^G = \frac{f_n}{f_b} = \mu \frac{\pi \rho g d}{E} \left(\frac{L}{t}\right)^3. \quad (3)$$

This analysis corresponds to a very dilute gas-like regime where the flexible beam only experiences collisions with isolated grains, such that we took $\alpha = 3$. Thus, the transition between straight and deformed configurations of the beam would occur at $c_Y \approx 1$ for a critical length

$$L_c^G \approx t \left(\frac{E}{\mu \pi \rho g d}\right)^{1/3}. \quad (4)$$

With the experimental parameters used in the present setup, we get $L_c^G \approx 7.5 \pm 0.5$ cm, i.e., below this length scale the flexible intruder should not experience bending reconfiguration.

However, as shown in Figs. 2 and 3, fully bent configurations were actually observed for much shorter fibers ($L = 3$ cm) than $L_c^G$. This diluted-regime argument thus underestimates the drag force exerted by the granular flow. To account for the effect of a denser liquid-like flow, one can consider the friction force associated with the grains present in the area that a slightly bent beam should sweep over to recover its initial straight shape. For a tip deflection of $\delta$, the swept area $\mathcal{A}_\delta$ is of the order of $\mathcal{A}_\delta \approx \delta L/2$ and the corresponding number of grains that are pushed back is $\phi \mathcal{A}_\delta / s$ where $s$ is the weighted average surface occupied by one grain on the bottom plate. The associated friction force will be $F_n = \mu \phi \rho g h \delta L/2$. Comparing this friction force $F_n$ to the elastic restoring force given by Eq. (2) with $\alpha = 8$, that is $F_b = 8EI\delta/L^3$ for an homogeneous and perpendicular loading on the whole fiber leads to

$$c_Y^L = \frac{F_n}{F_b} = \mu \frac{3\phi \rho g t}{4E} \left(\frac{L}{t}\right)^4, \quad (5)$$

and

$$L_c^L \approx t \left(\frac{4E}{3\mu \phi \rho g t}\right)^{1/4}, \quad (6)$$

which gives now a slightly lower value of the critical length, $L_c^L \approx 5.5 \pm 0.25$ cm for $\phi = 0.815$, but which remains much larger than the experimental observations despite the change of scaling exponent. This means, in particular, that the friction forces exerted by the grains are underestimated in the present argument.

Close to the jamming packing fraction, interactions of the flexible beam with the flow are actually expected to strongly alter the structure of the granular medium [43]. Transient jammed clusters can thus form in the vicinity of a wall [44] or a rigid intruder [27,28], and more generally by the application of shear stress [45].

In the present context, the elastic return of the deflected fiber to its straight conformation not only induces the displacement of the grains present in the swept-over area but also the building of a jammed cluster. The area of the latter can be estimated by a simple conservation argument analogous to the three-phase model developed for the accumulation of grains in front of a rigid obstacle [27,28]. We assume that the grains which are initially contained in the area $\mathcal{A}_\delta$ at the initial packing fraction $\phi$ and which are pushed back by the slightly bent fiber will all contribute to the formation of the jammed cluster. Therefore, for defining a criterion for bending or jiggling, we hypothesize that there is no recirculation of grains induced by the elastic return of the fiber and that the connected cluster of grains is at the homogeneous jamming packing fraction $\phi_J$ and is contacting the fiber upstream along its whole length. Thus the area $\mathcal{A}_J$ of the cluster that reaches the jamming packing fraction $\phi_J$ after it has absorbed the excess of grains swept over by the elastic fiber is

$$\mathcal{A}_J(\phi_J - \phi) = \mathcal{A}_\delta \phi = \frac{\delta L}{2}\phi. \quad (7)$$

In this close-to-jamming regime, we can thus build a Cauchy number with a drag force that results from the friction force of the jammed cluster, $F_J = \mu \rho g h \phi_J \mathcal{A}_J$. Here, the vicinity of the jamming density limit thus simply induces an amplification of the friction force by a factor $\phi_J/(\phi_J - \phi)$ so that we get for the Cauchy number

$$c_Y^J = \frac{\phi_J}{\phi_J - \phi} c_Y^L = \mu \frac{\phi \phi_J}{\phi_J - \phi} \frac{3\rho g t}{4E} \left(\frac{L}{t}\right)^4, \quad (8)$$

and for the critical length

$$L_c^J \approx t \left(\frac{\phi_J - \phi}{\phi \phi_J} \frac{4E}{3\mu \rho g t}\right)^{1/4}. \quad (9)$$

This critical length can be viewed as an elastogranular length as also defined in Ref. [35] in analogy with other works on elastocapillary phenomena [3].

The stability of the flexible beam thus appears to be controlled by two parameters: the rigidity (here the length) and the packing fraction of the granular medium. Using the value $\phi_J = 0.8356$ determined in Ref. [27], this leads, for an initial density $\phi = 0.815$ to $L_c^J \approx 2.2 \pm 0.1$ cm, a value that is more consistent with our experimental observations. In the phase diagram of Fig. 5 we see that the expression of the elastogranular length $L_c = L_c^J(\phi)$ from Eq. (9) gives indeed a reasonable account of the transition between the straight or deformed conformation of the fiber.

## IV. DEVELOPMENT OF THE TRANSITION

In contrast to the buckling instability, the switching of the flexible beam from its initial straight conformation to a bent one is gradual and requires reorganization of the granular medium. We focus here on the development of this transition.

A typical sequence (zoomed on the fiber) is shown in Fig. 6 for an intermediate fiber length $L = 3$ cm and a granular packing fraction $\phi = 80.94\%$. The initial location of the fiber is along the vertical of the figure ($Y$ axis). In a first stage, the fiber experiences only small lateral deflections and fluctuates around its straight initial position. For example, in Fig. 6(a), the fiber is slightly deflected on the left side and the lateral displacement of the free extremity is almost not visible. The granular material is still homogeneous, while grains are contacting the fiber on both sides. After a given traveling distance, the fiber bends irreversibly on one side with no possibility of returning back to its straight shape. While progressing inside the granular material, the fiber continues to bend [Fig. 6(b)] with a clear lateral deflection on the right side, indicated by the horizontal (red) arrow along the $X$ axis. Associated with this deflection,

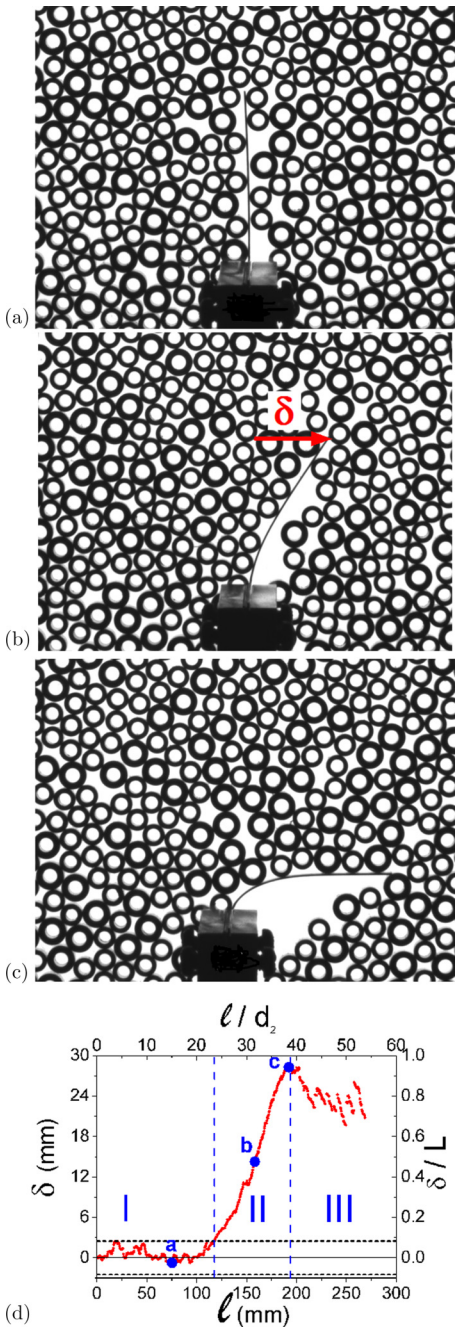


FIG. 6. Irreversible deflection of the bending fiber of length $L = 3$ cm in a granular medium of packing fraction $\phi = 80.94\%$ for different penetration distances $\ell$. (a) $\ell = 15.1d_2$, (b) $\ell = 31.7d_2$, (c) $\ell = 38.5d_2$. (d) Lateral deflection $\delta$ of the free fiber extremity as a function of the penetration distance $\ell$. The horizontal dotted lines represent the maximum excursion of $\delta$ during regime I. The three successive regimes I, II, and III are separated by the vertical blue dotted lines.

we clearly observe the appearance of a cavity downstream of the fiber. As the whole granular material still flows along the $Y$ axis, the fiber continues to bend and the free extremity might reach its maximum lateral deflection [Fig. 6(c)] when most of the fiber axis is placed perpendicularly to the initial flow. At this stage, the area of the cavity is larger. In the following we focus

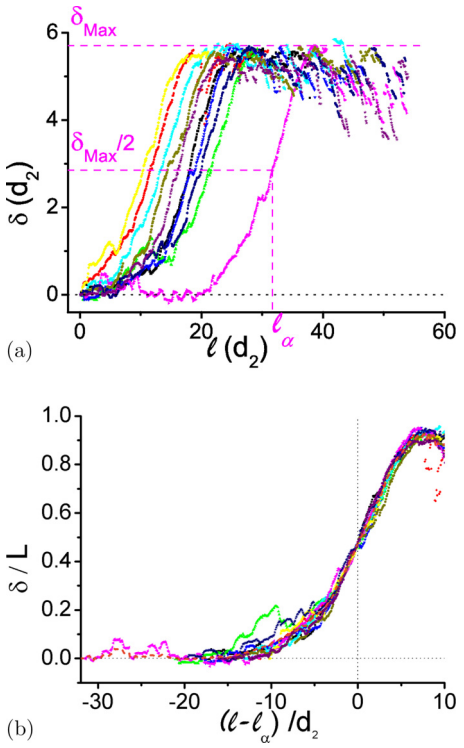


FIG. 7. (a) Lateral deflection $\delta$ of the free extremity of the fiber as a function of the plate displacement (or penetration distance) $\ell$ for 10 independent experiments performed with the same fiber length $L = 3$ cm and granular packing fraction $\phi = 80.94\%$. Both quantities are given in diameters of a large grain $d_2$. All the 10 curves reach the same maximal value $\delta_{\max}$, with $\ell_\alpha$ the penetration distance obtained for $\delta_{\max}/2$. (b) Same curves as in panel (a) expressed as a function of the reset penetration distance $\ell - \ell_\alpha$. The orange dashed curve is the average over the different experimental curves.

on this bifurcation in the penetration behavior by introducing some quantitative descriptors.

### A. Deflection of fiber tip

One way to quantitatively characterize the penetration of the fiber relative to the granular medium is to compute the lateral deflection $\delta$ (along the $X$ axis) of the free extremity of the fiber as a function of the distance $\ell$ traveled by the plate (or equivalently the displacement of the fiber anchoring point relative to the granular medium). The evolution of $\delta$ as a function of $\ell$ associated with the experiment shown in Figs. 6(a)–6(c) is shown in Fig. 6(d).

To give a more systematic account of this phenomenon, we report in Fig. 7 the evolution of the deflection $\delta$ as a function of the penetration distance $\ell$ expressed in diameters of a large grain ($d_2$) for ten independent experiments performed for a fiber length $L = 3$ cm and a granular packing fraction $\phi = 80.94\%$. At the end of an experiment, the fiber is observed to bend either toward the right (along $X > 0$) or toward the left side (along $X < 0$). To compare experiments, the $\delta$ values corresponding to experiments where the fiber eventually bends toward the left side have been inverted in Fig. 7, such that the final value of $\delta$ is always positive.

From Figs. 6, and 7 and from the corresponding experimental images, we recover the three stages identified above:

i. In a first regime (I), the lateral deflection $\delta$ is observed to fluctuate around zero. The fiber continuously penetrates the granular medium and keeps on average its initially straight shape. When the fiber is contacting grains at its tip, it is slightly deflected on one side or the other but the maximal amplitude of $\delta$ does not exceed the radius of a grain. Thus the extremity of the fiber experiences an erratic and fluctuating motion, depending on the local arrangement of the grains encountered by the fiber. There is only few interactions between the fiber and individual grains, and the wake left behind the fiber is reduced to a small elongated cavity almost not visible.

ii. After a penetration distance $\ell_1$ [indicated by the left vertical blue dotted line in Fig. 6(d)] that strongly depends on the realization, the fiber irreversibly bends towards one side (left or right). We checked the absence of bias in the direction of deflection. This regime II is characterized by a progressive and continuous bending of the fiber, shown by the regular increase of $\delta$ with the penetration distance $\ell$. This increase appears to be quite similar for the different experiments of Fig. 7.

iii. A third regime (III) appears when the extremity of the fiber roughly lies perpendicular to the direction of the plate translation $X$, i.e., $\theta(\xi = 1) \approx \pi/2$. Then the corresponding lateral deflection reaches its maximal value $\delta_{\max}$. For the examples of Fig. 7, the fiber then fluctuates around this new bent configuration. In the case of a pinned rigid fiber, the maximum possible value of the deflection would be $\delta_{\max} = L$. In our case, the anchoring point is clamped and the fiber is flexible. Then the observed $\delta_{\max}$ is slightly smaller than $L$, but has a constant value independent of $\phi$. For example, the average experimental values are $\delta_{\max} = (0.952 \pm 0.005)L$ for $L = 3$ cm.

As appears clearly in Fig. 7(a), we observe two fluctuating regimes separated by a transition that in contrast appears to be very deterministic. This deterministic aspect appears even more clearly in Fig. 7(b) after a resetting of the abscissa. Starting from the observation that the maximal deflection $\delta_{\max}$ only depends on the length of the fiber, we could indeed locate the traveling distance $\ell_\alpha$ corresponding to the deflection value $\frac{\delta_{\max}}{2}$, which is half of the average maximal deflection for each experiment $\alpha$. Then we could plot in Fig. 7(b) the deflection $\delta$ as a function of the reset penetration distance distance $\ell - \ell_\alpha$. The curves collapse rather well such that the average over the ten shifted experiments can be computed [Fig. 8(a)]. Interestingly the first part of the bending regime can be fit by an exponential growth [orange curve superimposed on the averaged experimental deflection in Fig. 8(a)]. The same plot is presented in a semilog scale in Fig. 8(b). This fit provides a characteristic length $\lambda$ for the kinetics of bending according to the formula $\delta = \delta_0 \exp(\ell/\lambda)$. For the example of Fig. 8, $\lambda = (4.89 \pm 0.04)d_2$. The length $\lambda$ has been obtained for all batches of experiments where bending occurred. Its value normalized by the $L_c$ value from Eq. (9) associated with the packing fraction $\phi$ is plotted in Fig. 9 (red circles) as a function of the rescaled fiber length, that is $\epsilon = \frac{L-L_c}{L_c}$. The $\epsilon$ value can be viewed as an order parameter: For $\epsilon < 0$, no irreversible bending occurs, the fiber stays in the jiggling regime, while for $\epsilon > 0$, bending occurs.

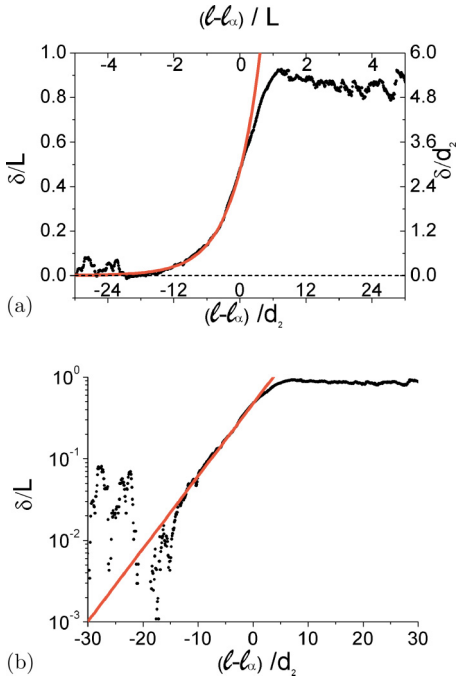


FIG. 8. Average of the lateral deflection $\delta$ of the free extremity of the fiber over the ten experiments of Fig. 7 as a function of the rescaled plate displacement $\ell - \ell_\alpha$. Both quantities are normalized by the diameter of a large grain $d_2$ (bottom and right axes) or by the fiber length (left and top axes). The orange curve is an exponential fit of the bending. (a) Normal scale; (b) semilog scale.

### B. Asymmetry of packing fraction

As clearly visible in Fig. 6, when the fiber enters the deflected regime and the lateral deflection is larger than a grain size, we observe the formation of a cavity empty of grains downstream of the fiber. A similar trend was observed in the framework of the penetration of a rigid obstacle in a granular layer [27].

Conversely, we expect an accumulation of grains, more specifically the formation of a jammed cluster, upstream of the fiber. Such an evolution is indeed observable in Fig. 10 where we present three successive snapshots of an experiment

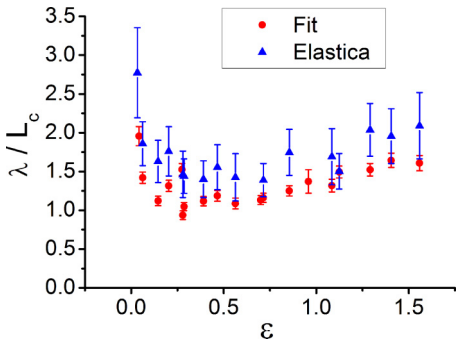


FIG. 9. Characteristic length scale $\lambda$ for the rate of bending as a function of $\epsilon = \frac{L-L_c}{L_c}$. Red circles are $\lambda$ values extracted from the exponential fit of deflection $\delta$ vs penetration distance $\ell$. Blue triangles are derived from the $A$ values of the compaction-induced bending model coupled with the elastica simulations.

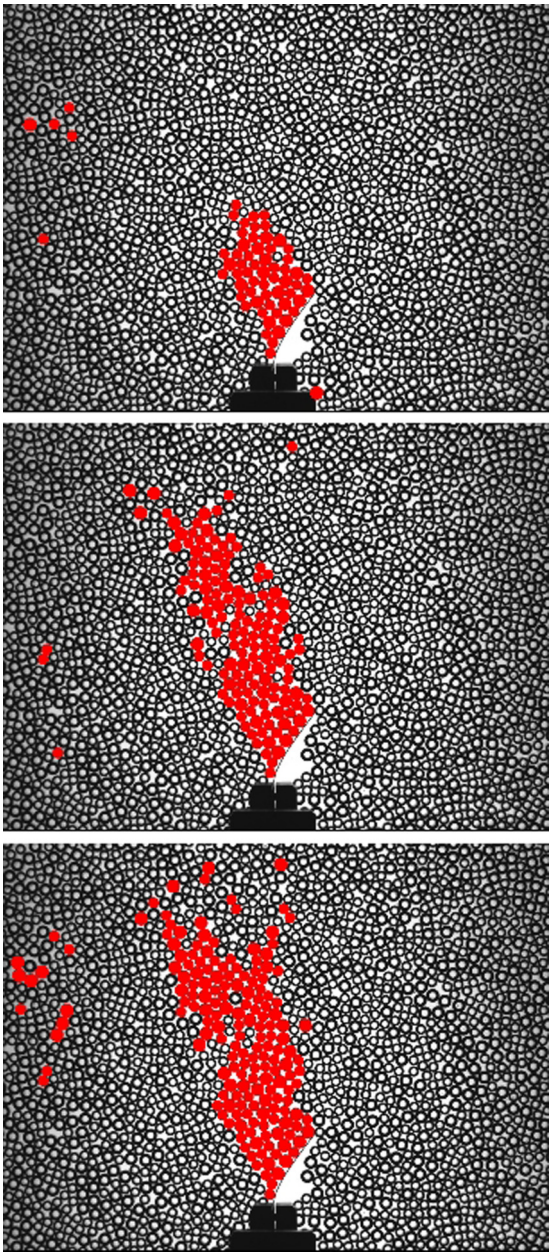

FIG. 10. Growth of a "cluster" of slow grains (red disk labeled) for three successive images starting from a penetration distance $\ell = 24.1 d_2$ for a granular packing at $\phi = 80.94\%$ and $L = 3$ cm.

of penetration of a fiber of length $L = 3$ cm in a granular medium of packing fraction $\phi = 80.94\%$.

In the present experiment, we recall that the anchoring point of the flexible intruder is fixed in the laboratory frame while the granular medium lies on a glass plate that is displaced at a constant velocity with $U_0$, the typical displacement of the plate between two successive images. The grains that accumulate upstream of the fiber are thus expected to be slowed down with respect to the mean flow. In Fig. 10, we show the distribution of the slowest (red disk labeled) grains, here selected on a simple threshold displacement criterion: We labeled the grains $i$ whose amplitudes of displacement between two successive images in the laboratory frame are $u_i < u_T = 0.048 U_0$. As expected, we observe a strong clustering of these slow grains upstream of

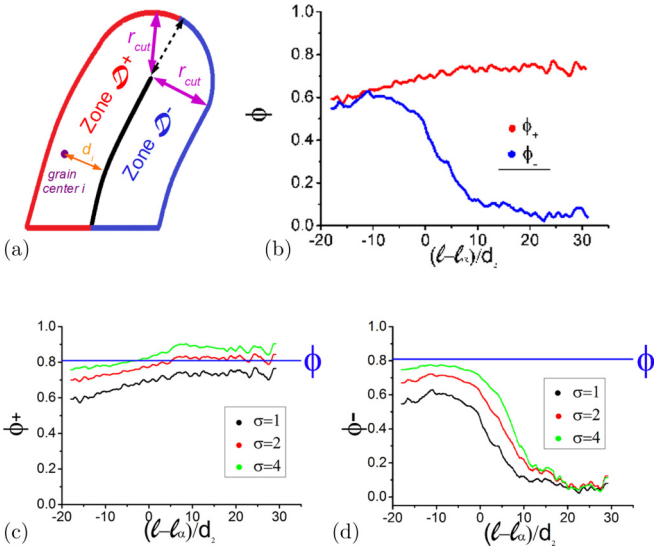


FIG. 11. Development of a packing fraction contrast between the two sides of the bending fiber. (a) Schematic diagram of the zones upstream and downstream of the fiber for calculation of $\phi_+$ (top curve) and $\phi_-$ (bottom curve). (b) Lateral packing fractions $\phi_+$ and $\phi_-$ (sliding window averaged over 10 points and over 10 experiments) as a function of the rescaled penetration distance $\ell - \ell_\alpha$ normalized by $d_2$ for a fiber length $L = 3$ cm in a granular medium with a macroscopic packing fraction $\phi = 80.94\%$ [indicated by the blue horizontal line in panels (c) and (d)]. Effect of the choice of the coarse-grained length scale $\sigma$ on the calculation of (c) $\phi_+$ and (d) $\phi_-$ (Increasing $\sigma$ from bottom to top curves).

the flexible beam. Although only qualitative, this observation supports the idea of the development of a jammed cluster of grains ahead of the fiber.

The penetration of the flexible beam in the granular medium thus leads to a clear symmetry breaking in the local packing fraction. To quantify this effect, we computed the coarse-grained packing fraction in the vicinity of the fiber.

Here we adapted the computation of the coarse-grained packing fraction [46] to define over a coarse-grained length scale $\sigma$ a left and a right packing fraction of grains on either side of the fiber. As sketched in Fig. 11(a), we define two domains $\mathcal{D}^+$ and $\mathcal{D}^-$ from either side of the fiber such that the distance of any point of a domain to the fiber remains below a cutoff value $r_{cut}$. The two packing fractions $\phi_+$ and $\phi_-$ are then computed as

$$\phi_\pm = \frac{1}{\alpha_\pm} \sum_{g_i \in \mathcal{D}^\pm} A_i \exp\left(-\frac{d_i^2}{\sigma^2}\right), \tag{10}$$

where $A_i$ is the area occupied by the grain $g_i$ and $d_i$ is its distance to the fiber. Here the parameter $\sigma$ is the coarse-graining length and we use $r_{cut} = 4\sigma$. The normalization factor $\alpha_\pm$ is obtained by the expression

$$\alpha_\pm = \int_{\vec{r} \in \mathcal{D}^\pm} \exp\left(-\frac{d(\vec{r})^2}{\sigma^2}\right) dx dy, \tag{11}$$

where $d(\vec{r})$ is the distance to the fiber of a point $\vec{r}$.

In Fig. 11(b), we show the evolution of the lateral packing fractions $\phi^+$ and $\phi^-$ obtained for a coarse-graining length

$\sigma = d_2$ after resetting the abscissa as in Fig. 7 by using the distance $\ell_\alpha$ and then averaging over 10 experiments. The bending transition appears very clearly to be accompanied by (i) a strong decrease of the downstream packing fraction $\phi^-$ down to values approaching zero, and (ii) a slight increase of the upstream $\phi^+$ up to a plateau value about $\phi^+_{\max} \approx 0.7$.

Note that this value is far lower than the jamming packing fraction of the present granular medium $\phi_J \approx 0.8356$ estimated in Ref. [27]. However, the value of the maximum packing fraction of a granular cluster is known to be significantly altered (decreased) in presence of a wall [47]. A clear illustration of this effect is given in Figs. 11(c) and 11(d) where we show the respective evolution of the upstream and downstream packing fractions $\phi^+$ and $\phi^-$ with increasing values of the coarse-graining length $\sigma$. We see that the larger the coarse-graining length, the larger the maximum upstream packing fraction $\phi^+$, which for $\sigma = 4d_2$ reaches a plateau value close to the expected jamming packing fraction.

By comparing Fig. 11(b) with Fig. 8, we observe that the symmetry breaking in the packing appears when the fiber deflection typically exceeds the half diameter of a grain. These results thus give a quantitative support to our phenomenological observations: the bending transition of the flexible beam is associated with a structural transition of the flowing granular medium with the formation of jammed cluster upstream of the fiber and the development of a cavity downstream of the fiber.

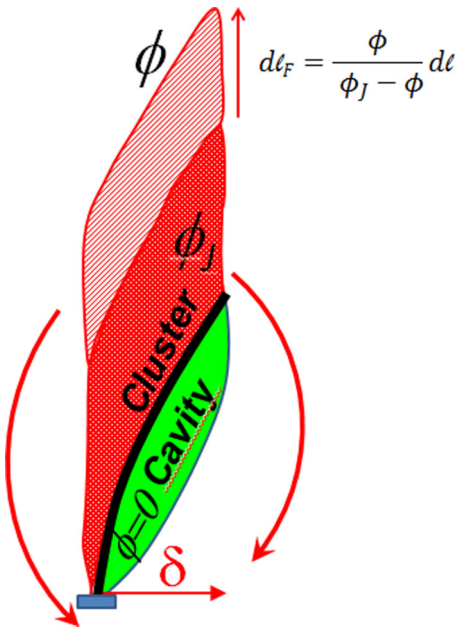


FIG. 12. Schematic diagram of the formation of a cluster at the jamming packing fraction $\phi_J$ ahead of the fiber and a cavity empty of grains behind the fiber. Aggregation of grains in front of the cluster through the advance of a compaction front and cluster erosion through recirculations of grains (red arrows) on both sides of the flexible intruder. The rest of the granular layer is at the packing fraction $\phi$.

## V. A SIMPLE MODEL OF BENDING-INDUCED COMPACTION

### A. Bending-induced compaction

As discussed in the previous section, the bending transition of the flexible beam is associated with an accumulation of grains upstream of the fiber, leading to the growth of a cluster at the jamming density $\phi_J$ as well as the development of a cavity empty of grains downstream of the fiber (see the schematic diagram of Fig. 12). The gradual bending of the flexible beam in the course of the penetration of the granular medium tends to increase the section of the intruder across the granular flow. We make the simple assumption that a larger intruder cross section collects a larger number of grains in the cluster. Thus the number of grains $dN_c{}^+$ entering the cluster for an infinitesimal penetration distance of $d\ell$ is assumed to be proportional to the deflection $\delta$ along $X$. This accumulation of grains in the cluster, which acts as a solid block connected to the fiber, increases the force acting against the elastic restoring force on the fiber.

In the spirit of the compaction front observed in the work of Waitukaitis *et al.* [48] and the three phase-model we developed for the penetration of a rigid intruder in a granular medium [27] we propose that the cluster grows faster for a packing fraction approaching the jamming transition. The compaction front (see Fig. 12) delimits the interface between the cluster at $\phi_J$ and the rest of the granular layer at $\phi$ in front of the fiber. For each penetration step $d\ell$, the compaction front advances over a distance of $d\ell_F$ greater than $d\ell$. Indeed there is an amplification factor linked to the approach to the jamming transition: $\frac{\phi}{\phi_J - \phi}$, thus resulting in $d\ell_F = \frac{\phi}{\phi_J - \phi} d\ell$ for a one-dimensional growth of the cluster as illustrated in Fig. 12. Therefore the number of grains arriving in the cluster will evolve as $\frac{dN_c{}^+}{d\ell} \propto \frac{\phi}{\phi_J - \phi}\delta$.

However, the compaction of a cluster of grains upstream of the fiber induces long-range effects in the granular medium [37,49]. In particular, it is accompanied here by recirculation flows on both sides of the intruder that tend to erode the cluster and convect grains downstream of the fiber. These recirculations are visible in the map of displacement fields of Fig. 4 in the plate frame, when the displacement of the plate has been subtracted from each grain displacement. In our previous work on the penetration of rigid intruders [28], it was observed that the lateral extent of recirculations was proportional to the diameter of the cylindrical intruder. Adapting this argument to the flexible intruder of spanwise length $\delta$ leads to a grain flux recirculating on both sides of the fiber which is proportional to $\delta$. The number of grains eroded from the cluster for each penetration step is thus expected to scale like $\frac{dN_c{}^-}{d\ell} \propto \delta$. Hence the evolution of the number of grains $N_c$ in the cluster is the balance of two terms: an accretion term and an erosion term that both depend on $\delta$ with $\frac{dN_c}{d\ell} = \frac{dN_c{}^+}{d\ell} - \frac{dN_c{}^-}{d\ell}$.

We assume that the friction force resulting from contacts between grains and between grains and fiber remains negligible with respect to the friction force resulting from the contact grains and the supporting plate. We also assume that, during bending the accretion term ($A^+$) is larger than the erosion term ($A^-$), such that the cluster grows and induces an increment of the friction force $F_c$ with $\frac{dF_c}{d\ell} \propto \frac{dN_c}{d\ell} \propto \delta$. During this transition regime we expect a quasistatic loading where the elastic force due to the bending $F_b$ compensates the friction

force induced by the jammed cluster of grains upstream of the fiber. This leads to the following evolution law:

$$\frac{dF_b}{d\ell} = A^+\delta - A^-\delta = A\delta. \tag{12}$$

Note that $A$ is a phenomenological parameter which has the dimension of pressure.

Given the knowledge of the constitutive relation $F_b(\delta)$ that relates the bending force of the flexible beam with its lateral deflection, Eq. (12) should thus give us an evolution law for the lateral deflection $\delta$ with respect to the penetration of the fiber $\ell$.

In the limit of small deflection and for a uniform perpendicular force density along the fiber, we can use the linear elasticity result $F_b = 8EI\delta/L^3$ and we get

$$\frac{d\delta}{d\ell} = \frac{A\,L^3}{8EI}\,\delta = \frac{\delta}{\lambda}. \tag{13}$$

We thus recover an exponential growth of the deflection of the fiber with respect to the penetration. This was observed experimentally in Fig. 8 where $\delta = \delta_0 \exp(\ell/\lambda)$ for the early stage of the bending. The identification of the exponential fit for the experimental values of $\delta$ with the evolution law of Eq. (13) gives the length $\lambda$, which characterizes the kinetics of bending:

$$\lambda = \frac{8EI}{AL^3}. \tag{14}$$

However, the experimental evolution of the deflection with penetration eventually shows a saturation which cannot be reproduced in the framework of the linear approximation of the elastic bending of the fiber, which is only valid for small deflection.

### B. Elastica

To account for the large deflection regime until the saturation behavior, we set up a nonlinear numerical model of our experimental system. The fiber is modeled by a unidimensional inextensible centerline parametrized in a 2D space by the rotation angle along the arc length between the local tangent of the deformed and undeformed curve. Our model is geometrically exact in the sense that there is no restriction on the amount of deflection the inextensible fiber can take (the geometrical limit is that self-interactions are not allowed in our model). The equilibrium configuration of the weightless fiber under an external density of force along its arc length is given by a 2D Kirchhoff equation [1]. To model the contacts of the grain on the fiber, we choose a density of forces that remains orthogonal to the fiber upon deformation (note that because of this nonconservative positional loading, the equilibrium equation cannot be derived from a mechanical energy formulation). Finally, we ensure a free boundary condition at one end and a torsional spring with a given stiffness on the other end to account for the possible imperfections of the experimental clamping.

Using finite differences [50], the second-order partial differential equilibrium equation is discretized in a set of $N$ nonlinear algebraic equations with $N$ unknowns that are the rotational degrees of freedom of the discretized structure. Here, $N$ is the number of discrete elements modeling the fiber that has been set to $N = 200$ to ensure numerical convergence. For a given discrete density of forces applied on the nodes of the discrete fibers, the equilibrium configuration is computed thanks to a classic Newton–Raphson algorithm. Note that the intensity of the density of forces has to be applied gradually from 0 to the desired intensity to ensure proper convergence of the Newton–Raphson algorithm. This numerical process gives us the nonlinear relation $F_b(\delta)$ that we were seeking.

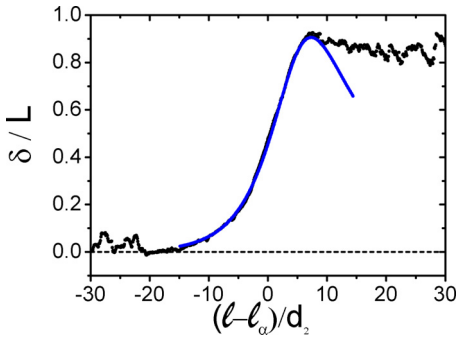


FIG. 13. Bending-induced compaction model (blue and smooth curve) superimposed on the experimental evolution of the averaged lateral deflection (black curve) as a function of the rescaled penetration distance with the same experimental parameters as in Fig. 7. The best $A$ value obtained from the model is $A = 2200 \pm 750$ Pa for this example.

As shown by the blue curve in Fig. 13, this computation now allows us to reasonably reproduce the full bending transition (regime II) of the fiber induced by the gradual compaction of grains upstream of the fiber. By tuning the value of $A$ to a given value, it is possible to reproduce the experimental evolution of deflection until its maximum value. The model does not allow us to reproduce the behavior beyond (regime III), in particular the plateau observed for this fiber length $L = 3$ cm, as the elastica calculations are based on the same type of loading whatever the deflection, i.e., an orthogonal repartition of forces along the whole fiber length. This strong assumption is certainly no more valid in regime III when the fiber adopts a hook shape; that is, when the angle $\theta(\xi = 1)$ exceeds $\pi/2$.

### C. Discussion of the model

The values of $A$ that match the curves of deflection like in Fig. 13 have been obtained for the different experiments performed with various fiber lengths $L$ or packing fractions $\phi$. For getting a physical meaning of $A$ in terms of length, we compute the corresponding $\lambda$ values from Eq. (14). The $\lambda$ value characterizes the typical penetration distance necessary to bend the fiber in regime II once the bifurcation occurs. In Fig. 9 these $\lambda$ values (blue triangles) are plotted as a function of the relative excess length above $L_c$; that is, $\epsilon = \frac{L-L_c}{L_c}$. The values of $\lambda$ (red circles) obtained from the direct fit $\delta = \delta_0 \exp(\ell/\lambda)$ of Fig. 8 are also plotted on the same curve for comparison. For both derivations, the $\lambda$ values are of the order of $L_c$ but both curves also exhibit the same complex and nonmonotonic evolution with $\epsilon$. For large $\epsilon$; that is, for long fibers, the $\lambda$ value seems to be governed by the excess length $L - L_c$. However, for $\epsilon \to 0$; that is, for fiber length approaching the critical length for bending, $\lambda$ increases by a factor of two.

For a fiber length just at the transition $L = L_c$ ($\epsilon = 0$) one would expect a divergence of $\lambda$, as $L_c$ provides the limit for the nonbending case. The increase of $\lambda$ observed for smaller $\epsilon$ might be interpreted in this framework. In any cases, Fig. 9 provides a intriguing relationship between $\lambda$, the length scale characterizing the rate of bending, and $L_c$, defining the critical fiber length for bending.

The elastica-derived model, although based on simple and minimal arguments, well captures the full range of the bending transition (regime II; Fig. 13), even if it cannot describe the deflection in regime III. More refined and complex loadings of the fiber (such as nonorthogonal forces or nonhomogeneous amplitudes or locations of point forces ...) might be investigated to improve the matching of the model with experimental deflections.

Moreover, even in bending regime II, the observed nonmonotonic evolution of $\lambda$ with $\epsilon$ probably indicates that there are two competing effects with increasing fiber lengths. Following the work of Ref. [34] on the buckling of elastic beams in granular media, it is tempting to consider that the fiber can be decoupled in two parts: one part of effective length $L_{\text{eff}}$ (probably related to $L_c$) that might supports the force exerted by the cluster, while the complementary part of length $L - L_{\text{eff}}$ would be simply led by the granular flow like a pinned rod. Direct measurements of forces and torques exerted on the fiber are needed to clearly identify the way the fiber is loaded. Complementary elastica simulations would provide a systematic way of quantifying the role of the fluctuating and discrete nature of force transmissions specific of granular material at the grain-fiber contacts. The approach to jamming introduces a further complex step in this new and intriguing fluid-structure interaction between and a flexible fiber and a dense granular flow.

## VI. CONCLUSION

This work presented a new fluid-structure interaction between a granular flow close to the jamming transition and a flexible fiber in a geometry of penetration. We identified a bending transition occurring for fiber longer than a characteristic length, which we call the elastogranular length $L_c$ as in the very recent work of Ref. [35]. In our case, the reconfiguration of the fiber shape was due to bending and not buckling but one can imagine promoting mechanisms of buckling by progressively increasing the aspect ratio between the fiber thickness and the grain diameter.

The bending transition was associated with a symmetry breaking in the packing fraction, with the formation of a cluster upstream of the fiber and a cavity empty of grains downstream of the fiber. We proposed an expression for $L_c$ that combines both rigidities of the flexible fiber and granular material approaching the jamming transition. The elastogranular length $L_c$ controlled the transition between the bending and jiggling regimes for the fibers embedded in the granular medium. But surprisingly, $L_c$ was also observed to determine the kinetics of the bending once the transition started.

## ACKNOWLEDGMENTS

We acknowledge the crucial technical help of T. Darnige as well as enlightening discussions with P. Gondret and A. Seguin. We also acknowledge all the students who have contributed to this work: Marguerite Leang, Yuka Takehara (from the group of K. Okumura), François Postic as well as Katherin Luginbuhl, Dawn Wendell and Nadia Cheng from the group of A. Hosoi through the MIT-France Seed Fund/MISTI Global Seed Fund project for the year 2009-2010 on "Flexible Objects in Granular Media."

[1] B. Audoly and Y. Pomeau, *Elasticity and Geometry: From Hair Curls to the Nonlinear Response of Shells* (Oxford University Press Inc., New York, 2010).
[2] Z. Bazant and L. Cedolin, *Stability of Structures: Elastic, Inelastic, Fracture and Damage Theories* (World Scientific Publishing Co. Pte. Ltd., Singapore, 2010).
[3] B. Roman and J. Bico, J. Phys.: Condens. Matter **22**, 493101 (2010).
[4] M. J. Shelley and J. Zhang, Annu. Rev. Fluid Mech. **43**, 449 (2011).
[5] A. Lindner and M. Shelley, *Fluid-Structure Interactions in Low-Reynolds-Number Flows* (Royal Society of Chemistry, 2015), pp. 168–192.
[6] S. Ramananarivo, R. Godoy-Diana, and B. Thiria, Proc. Natl. Acad. Sci. USA **108**, 5964 (2011).
[7] F. Gosselin, E. de Langre, and B. A. Machado-Almeida, J. Fluid Mech. **650**, 319 (2010).
[8] L. Schouveiler and A. Boudaoud, J. Fluid Mech. **563**, 71 (2006).
[9] S. Alben, M. Shelley, and J. Zhang, Nature (London) **420**, 479 (2002).
[10] S. Vogel, *Life in Moving Fluids: The Physical Biology of Flow* (Princeton University Press, 1994).
[11] N. Coq, O. du Roure, J. Marthelot, D. Bartolo, and M. Fermigier, Phys. Fluids **20**, 051703 (2008).
[12] J. Xiao and X. Chen, J. R. Soc., Interface **10**, 0399 (2013).
[13] M. K. Jawed, N. K. Khouri, F. Da, E. Grinspun, and P. M. Reis, Phys. Rev. Lett. **115**, 168101 (2015).
[14] E. de Langre, A. Gutierrez, and J. Cosse, C. R. Mec. **340**, 35 (2012).
[15] M. Luhar and H. M. Nepf, Limnol. Oceanogr. **56**, 2003 (2011).
[16] S. Barsu, D. Doppler, J. J. S. Jerome, N. Rivière, and M. Lance, Phys. Fluids **28**, 107101 (2016).
[17] G. C. Buster, M. R. Laufer, and P. F. Peterson, Nucl. Eng. Des. **303**, 153 (2016).
[18] E. Kolb, C. Hartmann, and P. Genet, Plant Soil **360**, 19 (2012).
[19] D. M. Wendell, K. Luginbuhl, J. Guerrero, and A. E. Hosoi, Exp. Mech. **52**, 945 (2012).
[20] A. E. Hosoi and D. I. Goldman, Ann. Rev. Fluid Mech. **47**, 431 (2015).
[21] R. Albert, M. A. Pfeifer, A. L. Barabási, and P. Schiffer, Phys. Rev. Lett. **82**, 205 (1999).
[22] I. Albert, J. G. Sample, A. J. Morss, S. Rajagopalan, A.-L. Barabási, and P. Schiffer, Phys. Rev. E **64**, 061303 (2001).
[23] M. B. Stone, R. Barry, D. P. Bernstein, M. D. Pelc, Y. K. Tsui, and P. Schiffer, Phys. Rev. E **70**, 041301 (2004).
[24] R. Candelier and O. Dauchot, Phys. Rev. Lett. **103**, 128001 (2009).
[25] R. Candelier and O. Dauchot, Phys. Rev. E **81**, 011304 (2010).

[26] A. Fiege, M. Grob, and A. Zippelius, Granular Matter **14**, 247 (2012).
[27] E. Kolb, P. Cixous, N. Gaudouen, and T. Darnige, Phys. Rev. E **87**, 032207 (2013).
[28] E. Kolb, P. Cixous, and J. C. Charmet, Granular Matter **16**, 223 (2014).
[29] A. Seguin, Y. Bertho, F. Martinez, J. Crassous, and P. Gondret, Phys. Rev. E **87**, 012201 (2013).
[30] A. Seguin, C. Coulais, F. Martinez, Y. Bertho, and P. Gondret, Phys. Rev. E **93**, 012904 (2016).
[31] A. H. Clark, L. Kondic, and R. P. Behringer, Phys. Rev. E **93**, 050901(R) (2016).
[32] R. A. L. de la Cruz and G. A. Caballero-Robledo, J. Fluid Mech. **800**, 248 (2016).
[33] A. Merceron, A. Sauret, and P. Jop, Phys. Rev. E **93**, 062904 (2016).
[34] A. R. Mojdehi, B. Tavakol, W. Royston, D. A. Dillard, and D. P. Holmes, Extreme Mech. Lett. **9**, 237 (2016).
[35] D. J. Schunter Jr., M. Brandenbourger, S. Perriseau, and D. P. Holmes, arXiv:1706.07849.
[36] N. Algarra, M. Leang, A. Lazarus, D. Vandembroucq, and E. Kolb, EPJ Web Conf. **140**, 14002 (2017).
[37] M. Bouzid, A. Izzet, M. Trulsson, E. Clément, P. Claudin, and B. Andreotti, Eur. Phys. J. E: Soft Matter Biol. Phys. **38**, 125 (2015).
[38] F. Radjai and S. Roux, Phys. Rev. Lett. **89**, 064302 (2002).
[39] G. Combe, V. Richefeu, G. Viggiani, S. A. Hall, A. Tengattini, and A. Atman, AIP Conf. Proc. **1542**, 453 (2013).
[40] K. Saitoh and H. Mizuno, Soft Matter **12**, 1360 (2016).
[41] P. Cixous, Ph.D. thesis, Université Pierre et Marie Curie - Paris VI, 2009, https://pastel.archives-ouvertes.fr/pastel-00622262/file/pierre_cixous_final.pdf.
[42] A. Boudaoud, P. Patricio, Y. Couder, and M. Ben Amar, Nature (London) **407**, 718 (2000).
[43] P. Mills, P. G. Rognon, and F. Chevoir, Europhys. Lett. **81** 64005 (2008).
[44] P. G. Rognon, T. Miller, B. Metzger, and I. Einav, J. Fluid Mech. **764**, 171 (2015).
[45] D. Bi, J. Zhang, B. Chakraborty, and R. P. Behringer, Nature (London) **480**, 355 (2011).
[46] C. Goldenberg, A. Tanguy, and J.-L. Barrat, Europhys. Lett. **80**, 16003 (2007).
[47] K. W. Desmond and E. R. Weeks, Phys. Rev. E **80**, 051305 (2009).
[48] S. R. Waitukaitis, L. K. Roth, V. Vitelli, and H. M. Jaeger, Europhys. Lett. **102**, 44001 (2013).
[49] K. A. Reddy, Y. Forterre, and O. Pouliquen, Phys. Rev. Lett. **106**, 108301 (2011).
[50] A. Lazarus, J. T. Miller, and P. M. Reis, J. Mech. Phys. Solids **61**, 1712 (2013).